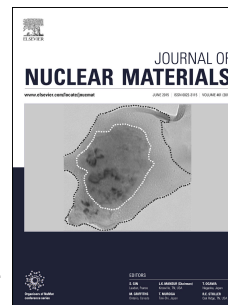


Accepted Manuscript

Discovery of a maximum damage structure for Xe-irradiated borosilicate glass ceramics containing powellite

Karishma B. Patel, Sylvain Peugot, Sophie Schuller, Giulio I. Lampronti, Sébastien P. Facq, Clara Grygiel, Isabelle Monnet, Ian Farnan



PII: S0022-3115(18)30585-3

DOI: [10.1016/j.jnucmat.2018.08.012](https://doi.org/10.1016/j.jnucmat.2018.08.012)

Reference: NUMA 51135

To appear in: *Journal of Nuclear Materials*

Received Date: 24 April 2018

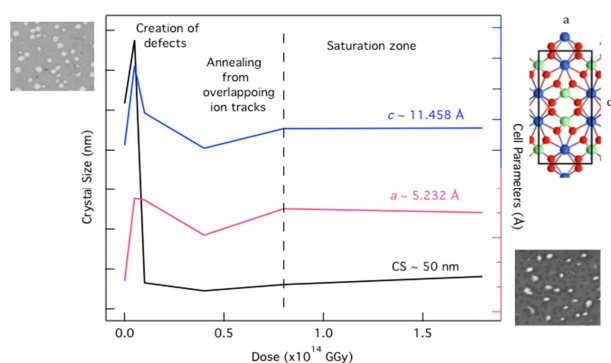
Revised Date: 17 July 2018

Accepted Date: 6 August 2018

Please cite this article as: K.B. Patel, S. Peugot, S. Schuller, G.I. Lampronti, Sé.P. Facq, C. Grygiel, I. Monnet, I. Farnan, Discovery of a maximum damage structure for Xe-irradiated borosilicate glass ceramics containing powellite, *Journal of Nuclear Materials* (2018), doi: 10.1016/j.jnucmat.2018.08.012.

This is a PDF file of an unedited manuscript that has been accepted for publication. As a service to our customers we are providing this early version of the manuscript. The manuscript will undergo copyediting, typesetting, and review of the resulting proof before it is published in its final form. Please note that during the production process errors may be discovered which could affect the content, and all legal disclaimers that apply to the journal pertain.

Graphical Abstract (TOC)



Keywords: radiation effects, nuclear waste materials, glass ceramics, molybdenum encapsulation.

Highlights:

- Radiation response of CaMoO_4 bearing glasses examined using XRD, SEM and Raman
- Minor amorphization of crystallites detected, but bulk of particles show resistance
- Modifications to crystallinity and amorphous network saturate for doses $> 4 \times 10^{13}$ ions/cm²
- Saturation caused by competing processes of damage creation and thermal recovery

Discovery of a maximum damage structure for Xe-irradiated borosilicate glass ceramics containing powellite

Karishma B. Patel^{††}, Sylvain Peugot[□], Sophie Schuller[∞], Giulio I. Lampronti[†], Sébastien P. Facq[†], Clara Grygiel[§], Isabelle Monnet[§], Ian Farnan[†]*

[†] Department of Earth Sciences, University of Cambridge, Downing Street, Cambridge, CB23EQ, UK

[□] CEA, DEN, DE2D, SEVT, LMPA, Marcoule, F-30207 Bagnols-sur-Cèze, France

[∞] CEA, DEN, DE2D, SEVT, LDPV, Marcoule, F-30207 Bagnols-sur-Cèze, France

[§] CIMAP CEA/CNRS/ENSICAEN/Normandie Université, Boulevard Henri Becquerel BP5133, 14070, Caen cedex 5, France

ABSTRACT In order to increase the waste loading efficiency in nuclear waste glasses, alternate glass ceramic (GC) materials are sought that trap problematic molybdenum in a water-durable CaMoO_4 phase within a borosilicate glass matrix. In order to test the radiation resistance of these candidate wastefoms, accelerated external radiation can be employed to replicate long-term damage. In this study, several glasses and GCs were synthesized with up to 10 mol% MoO_3 and subjected to 92 MeV Xe ions with fluences ranging between 5×10^{12} to 1.8×10^{14} ions/cm². The main mechanisms of modification following irradiation involve: (i) thermal and defect-assisted diffusion, (ii) relaxation from the ion's added energy, (iii) localized damage recovery from overlapping ion tracks, and (iv) the accumulation of point defects or the formation of voids that created significant strain and led to longer-range modifications. Most significantly, a saturation in alteration could be detected for fluences greater than 4×10^{13} ions/cm², which represents an average structure that is representative of the maximum damage state from these competing mechanisms. The results from this study can therefore be used for long-term structural projections in the development of more complex GCs for nuclear waste applications.

1.0 Introduction

In order to increase waste loading efficiency in nuclear waste glasses, alternate glass ceramic (GC) compositions are receiving a resurgence of interest as the use of civil nuclear reactors continues to grow. These structures are a useful alternative as they utilize an amorphous matrix to encapsulate the majority of shorter-lived radioisotopes, while enabling actinides and poorly soluble waste components such as sulfates, chlorides, and molybdates to be contained in a more durable crystalline phase [1–3]. These composite materials are of industrial interest for future wasteforms as they can reduce the final volume of waste for storage in a geological repository, accommodate waste from fuel with a higher burn-up thus increasing fuel efficiency, or be used for existing waste streams high in insoluble species, such as those arising from post-operation clean out or legacy waste from military applications.

Vitrification of high-level nuclear waste (HLW) into a glass is the widely accepted technique used for the immobilization of radioisotopes [4,5], as glasses show good thermal and radiation resistance, chemical durability when exposed to aqueous environments, and they can incorporate a wide variety of radioisotopes [1,5,6]. While there are many benefits to using these structures for long-term radioisotope storage, waste loading is limited to ~ 18.5 wt% in French nuclear waste glass R7T7 [7] in order to prevent phase separation [3,8,9], which can lead to a degradation of the wasteform's physical properties [2,10]. Molybdenum is a particularly problematic fission product that limits waste loading, as it can lead to the crystallization of water-soluble alkali molybdates (Na_2MoO_4 , Cs_2MoO_4), known as yellow phase [9,11]. Yellow phase can act as a carrier for radioactive cesium and strontium [1,12], and hence its formation can severely alter the safety case for geological storage. While alkali molybdates are undesired, alkaline earth molybdates such as CaMoO_4 are comparatively water-durable (13,500 x less

soluble than alkali molybdates [13]), and can therefore be used to trap insoluble molybdenum into a stable phase within a borosilicate glass matrix. Simplified GCs limiting the formation of Na_2MoO_4 relative to CaMoO_4 have been successfully synthesized [9,14–16], but more important to determine is the radiation response of these composite frameworks given that nuclear waste will undergo internal radioactive decay for millennia.

Accumulated radiation damage created during the encapsulation of radioisotopes can alter the composition and structure of both crystalline and amorphous phases, which can therefore affect the long-term durability of any glass or composite wasteforms. Internal radiation created by α -decay of minor actinides and Pu, β -decay of fission products, and transitional γ -decay processes can cause atomic displacements, ionization, and electronic excitations. In glasses, these events can result in changes to volume and mechanical properties, composition, stored energy, and can also induce phase transformations, such as devitrification, bubble formation, glass-in-glass phase segregation, or clustering of cations [4,5,17,18]. The range of effects is dependent on composition [19] and can sometimes result in favorable properties, such as an increase in fracture toughness, or re-vitrification of unwanted crystalline phases [4,5]. In crystals, radiation can cause a similar range of effects, in addition to causing significant dislocation within the crystal lattice and possible amorphization [20,21].

The α -decay process, and specifically the heavy recoil nuclei, is theorized to be responsible for the greatest disruption of structural order, and hence the bulk of observed macroscopic changes [4,5]. This α -recoil (70 – 100 keV) interacts primarily through ballistic collisions resulting in atomic displacements, while the high-energy α -particle (He^{2+}) interacts predominantly through electronic collisions that can initiate recovery processes through the creation of latent ion tracks [4,5,22]. A generally accepted model used to describe this process is the thermal spike model, in

which energy is transferred to the host lattice's electrons via electron-electron and electron-phonon coupling. These interactions translate into a small cylinder of energy characterized by a temperature of ~ 1000 K [23]. Theoretically, electronic stopping can lead to defect annealing, or structural reorganization and precipitate formation. Thermal spikes associated with high electronic energy loss will lead to damage generation through the creation of ion tracks, while lower electronic energy loss can cause damage recovery.

Experimentally, borosilicate glasses subjected to irradiation have thus far remained amorphous, but some changes to mechanical properties, internal energy, and density properties have been observed [4,24]. Interestingly, a saturation in property modifications could be detected for irradiation doses between 2 to 4 $\times 10^{18}$ α/g [5,19]. A similar saturation in structural modifications has also been observed in MD simulations [25], which further supports the formation of an equilibrium state when the processes of defect formation occur at a rate similar to that of self-healing from overlapping ion tracks. Given current waste loading standards and waste streams, this saturation in structural modifications is expected to occur following ~ 1000 years of storage [4,5,24]. By replicating the damage occurring within this timeframe, it is therefore possible to estimate long-term damage structures. This knowledge is essential for the evaluation of any candidate materials for nuclear waste storage.

In this paper, the damage predicted to occur around this 1000 year timeframe is replicated to assess the durability of GCs with CaMoO_4 crystallites embedded in a borosilicate matrix. It is a fundamental approach that mimics the effects α -decay using external swift heavy ion (SHI)-irradiation in compositions that are simplified to components known to affect the formation of CaMoO_4 [26,27]. This study attempts to identify if long-term radiation damage will: (i) induce phase separation in homogenous systems, (ii) propagate existing phase separation, (iii) cause

remediation of glass-in-glass phase separation or amorphization of crystallites through local annealing, or (iv) some combination of the above. It further seeks to identify if the saturation in modifications observed for homogeneous systems can also be detected in GCs. It therefore attempts to provide long-term structural projections of alternative nuclear waste materials in an effort to develop wastefoms with a higher waste loading efficiency that are equally resistant to internal radiation damage.

2.0 Materials and experimental methodology

2.1 Composition and synthesis techniques

For this study a series of non-active glasses and glass ceramics (GCs) were synthesized to test the formation and durability of powellite (CaMoO_4) within a borosilicate glass network when the materials were subjected to external radiation. The normalized glass and GC compositions are given in Table 1. In order to trap molybdenum in a powellite phase, MoO_3 was added in a 1:1 ratio to CaO in a borosilicate glass normalized to SON68 (non-active form of R7T7) with respect to SiO_2 , B_2O_3 and Na_2O . A simplified borosilicate glass was also prepared to test the glass-in-glass phase separation tendencies induced by irradiation in systems without molybdenum. In most cases, compositions also included 0.15 mol% Gd_2O_3 . Gadolinium can act as an actinide surrogate, and therefore it can serve as a marker for incorporation of active species within either the glassy or crystalline phase. One GC did not include gadolinium in order to differentiate changes to crystallization processes following external irradiation in systems with and without a dopant.

Table 1. Sample composition in mol%.

Sample	SiO_2	B_2O_3	Na_2O	CaO	MoO_3	Gd_2O_3
CNO	63.39	16.88	13.70	6.03	-	-

CNG1	61.94	16.49	13.39	7.03	1.00	0.15
CNG1.75	60.93	16.22	13.17	7.78	1.75	0.15
CNG2.5	59.93	15.96	12.95	8.52	2.50	0.15
CNG7	53.84	14.34	11.64	13.03	7.00	0.15
CN10	49.90	13.29	10.78	16.03	10.00	-

Glass batches of ~ 30 g were prepared using a double melt of SiO₂, H₃BO₃, Na₂B₄O₇, Na₂CO₃, CaCO₃, MoO₃ and Gd₂O₃ powders in air within a platinum/ruthenium crucible heated to 1500°C. The first melt was held for 30 min, after which samples were crushed and re-melted for 20 min to ensure homogeneity of element distribution. Melts were then cast at room temperature on a graphite-coated iron plate and annealed for 24 h at 520°C.

For the irradiation experiments, samples were cut to a thickness of 1 mm with surface dimensions of ~ 4 mm × 4 mm tailored to fit the beamline sample holder. Each piece was hand polished successively with P600, 800, 1200, 2400 and 4000 SiC grit paper, followed by 3 μm and 1 μm diamond polishing to achieve a thickness of approximately 500 μm and a surface apt for analytical techniques.

2.2 Irradiation experiment

External SHI-irradiation can be used to replicate the damage state induced by electronic and nuclear collisions resulting from internal α-decay processes on an accelerated scale in waste glasses [4,26,28]. It is predicted that a similar series of damage processes will occur in glass ceramics from accumulated ion tracks, though there are yet no active implanted experiments to verify this hypothesis. However, the high ion energies and fluences achieved through SHI-irradiation will create significant disorder indicative of the maximum possible damage resulting during long-term storage.

In this experiment, 92 MeV Xe²³⁺ ions, with an average flux of 2.3×10^9 ions/cm²·s were used to irradiate five different sample sets with fluences of 1.8×10^{14} , 8×10^{13} , 4×10^{13} , 1×10^{13} , and 5×10^{12} ions/cm² on the IRRSUD beamline in Ganil. According to TRIM calculations [29], this resulted in an estimated penetration depth of ~ 12 μm (see Supplementary Information A1.1 for plots of energy losses with depth).

Multiple fluences were collected in order to provide information on the origins of structural transformations, as well as testing if a saturation in structural modifications could be detected. In homogeneous sodium borosilicate glasses, this saturation occurs for fluences around 1×10^{13} ions/cm² for high-energy ions, and around 1×10^{14} ions/cm² for low-energy (keV scale) ions, which is roughly equivalent to ~ 1000 years of storage given current waste loading standards [5,19]. Therefore, the fluences achieved in this study should be able to detect a plateau in modifications, if one exists for these composite compositions.

2.3 Characterization techniques

The mechanisms of structural modification following irradiation were investigated using several analytical techniques in order to characterize changes occurring in both the amorphous and crystalline phases. Morphology, composition, and crystal phase and size determination were examined using X-ray diffraction (XRD) and Scanning Electron Microscopy (SEM), while changes to bonding was investigated using Raman spectroscopy. Together these techniques were able to assess the bulk and phase specific response to irradiation, as well as determining if any cationic substitution into powellite or additional precipitation took place.

XRD was performed with CuK _{α 1} ($\lambda = 0.15406$ nm) and CuK _{α 2} ($\lambda = 0.15444$ nm) wavelengths on a Bruker D8 ADVANCE equipped with Göbel mirrors for a parallel primary beam and a Vautec position sensitive detector. Spectra were collected for a $2\theta = 10 - 90^\circ$ range with a 0.02°

step size and 10 s per step dwell time. Samples were analyzed as monoliths to isolate irradiation effects at the surface, and rotated to find the maximum diffracting orientation before final acquisition, as a means to compare samples containing randomly orientated crystals with some accuracy. Structural analysis and Scherrer crystallite size (CS) valuations were performed using whole pattern Rietveld refinements with the software Topas v4.1 [30]. A single parameter approach was utilized based on the quality of data and large amorphous content, as has been thoroughly discussed elsewhere [14,31]. In this fitting method, CS is presumed to incorporate contributions from both size and strain, as correlation issues prevented the independent deconvolution and quantification of these two physical properties.

SEM backscattered electron (BSE) imaging and energy dispersive X-ray spectroscopy (EDS) were performed on a FEI Quanta-650F operating at low vacuum (0.06 – 0.08 mbar) or in environmental scanning electron microscopy (ESEM) mode (0.10 mbar) with a 5 – 7.5 keV beam and a 40 μm aperture. This configuration resulted in a penetration depth of $\sim 1 \mu\text{m}$. EDS results were collected using a 8 mm cone in order to reduce skirting effects, thus providing information on the relative composition of each identifiable phase. Six to ten measurements were collected for each phase and then averaged to provide statistical certainty. Owing to the heterogeneous nature of the samples and the need for comparison, ratios were used as a metric between phases, instead of absolute values. Images were collected using FEI Maps software, while acquisition and analysis for EDS was performed using Bruker ESPRIT software. Quantification of particle size and density at the surface were determined by image analysis using ImageJ.

Raman spectroscopy was a complementary analytical method to the aforementioned techniques, as it is able to determine changes to the local environment induced by irradiation in

both crystalline and non-diffracting amorphous phases. Raman spectra were collected with a 300 μm confocal Horiba Jobin Yvon LabRam300 spectrometer equipped with a holographic grating of 1800 grooves per mm and coupled to a Peltier cooled front illuminated CCD detector resulting in a spectral resolution of $\sim 1.4 \text{ cm}^{-1}$ per pixel (1024×256 pixels in size). The excitation line at 532 nm was produced using a diode-pumped solid-state laser (Laser Quantum) with an incident power of 100 mW focused on the sample with an Olympus 50x objective. Spectra were collected over the $150 - 1600 \text{ cm}^{-1}$ range with a $2 \mu\text{m}$ spot size. The given equipment configuration resulted in an estimated penetration depth of $\sim 22 \mu\text{m}$, based on depth profile analysis. While this set-up still results in a contribution from the pristine layer under the irradiation zone, the parameters chosen were based on a number of factors including acquisition time, spectral resolution, minimization of damage, and desire to describe the amorphous phase. Multiple acquisitions (3 - 4) were made for each sample to provide some reliability, and all spectra were analyzed using PeakFit software, where characteristic bands were fit with pseudo-voigt profiles.

3.0 Results

3.1 Pristine samples

The synthesized GCs (CNG1.75, CNG2.5, CNG7, and CN10) successfully prevented the formation of Na_2MoO_4 for up to 10 mol% MoO_3 in a soda lime borosilicate glass, with a MoO_3 solubility limit around 1 mol%, as previous works have indicated [14]. In these GCs, CaMoO_4 crystallites form particles that are free of gadolinium substitution and are evenly distributed within a homogeneous glassy matrix. The particle size (PS) for these GCs is proportional to $[\text{MoO}_3]$ with two groups of PS and CS identified by SEM and XRD, respectively. One PS is in the range of 200 – 400 nm with CS $\sim 50 \text{ nm}$ for $[\text{MoO}_3] \leq 2.5 \text{ mol\%}$. The other PS is in the range of 0.5 – 1.0 μm with CS $\sim 140 \text{ nm}$ for $[\text{MoO}_3] \geq 7 \text{ mol\%}$.

In samples with $[\text{MoO}_3] \leq 1$ mol% or without molybdenum, the systems were homogeneously amorphous and single phased as characterized by a homogeneous grey surface through SEM imaging. Furthermore, no diffraction peaks or crystalline Raman bands could be detected in these glasses. Additional images and spectra for pristine samples are detailed elsewhere [14].

3.2 Morphology and composition following irradiation

Following Xe-irradiation, the amorphous samples CNO and CNG1 remained fully amorphous according to all analytical techniques used in this experiment, while CaMoO_4 free of any Na-Gd substitution was the only detectable crystalline phase in GCs according to XRD, SEM and Raman spectroscopy results.

For GCs with $[\text{MoO}_3] \leq 2.5$ mol%, the size of particles remained fairly constant within a 200 – 450 nm range following irradiation, indicating the durability of the crystalline phase. There was however a shift to smaller, but more populous particles for a fluence of 8×10^{13} ions/cm² (Figure 1 (e)). At this fluence, the size range of particles decreased by ~ 100 nm, but the number of particles increased by roughly $3 \times$ that observed in the unirradiated sample. It is hypothesized that changes within the amorphous network, such as local viscosity changes or a reduction in stress induced during synthesis enabled particle constituents to migrate or crystallites to dissolve into the bulk, thus resulting in the observed changes to particle size and distribution.

The non-uniform PS changes observed with respect to dose could be a result of pre-existing differences in poured GCs. Alternatively they could be a result of radiation-induced relaxation of local stresses or competing processes of amorphization and re-precipitation, which have a dependence on dose. As a similar anomaly of smaller, but more populous particles was also observed for CNG2.5, it implies that radiation damage or the high electric current induced by external SHI-irradiation at the surface is likely causing this change in microstructure, as opposed

to sampling. Given that the scale at which these changes occurred is reaching the SEM detection limits, the key consideration to note is that some migration or dispersion of crystallites is detected, but that these changes to PS following SHI-irradiation are minor for compositions with low MoO₃, as Figure 1 indicates.

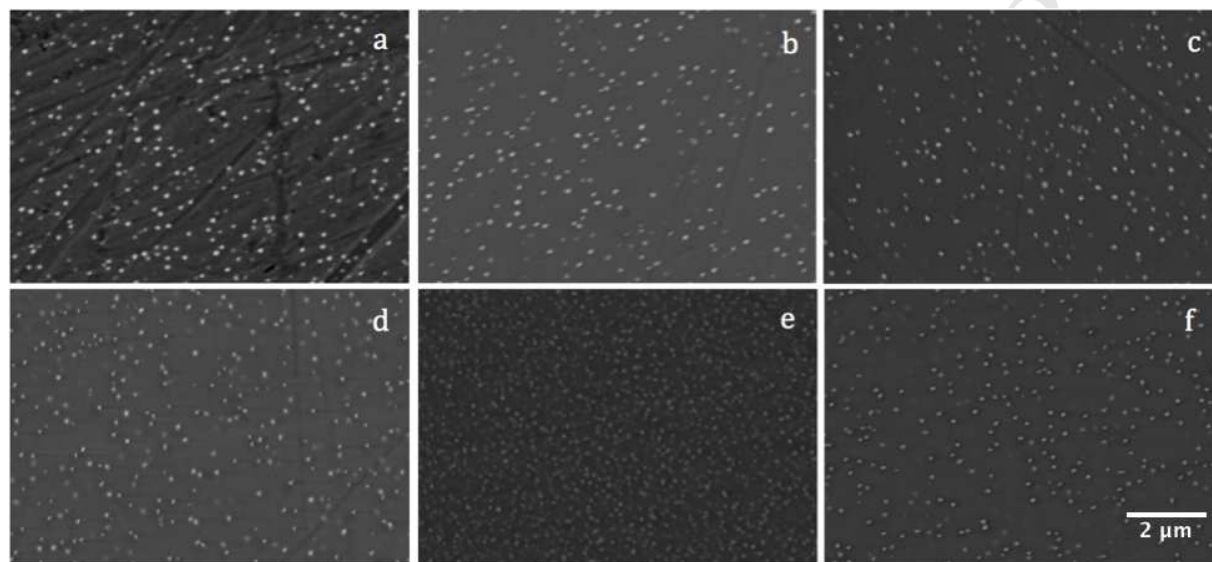


Figure 1. BSE images of CNG1.75 at (a) pristine conditions, and following Xe-irradiation with fluences of: (b) 5×10^{12} , (c) 1×10^{13} , (d) 4×10^{13} , (e) 8×10^{13} , and (f) 1.8×10^{14} ions/cm². The particle densities determined by image analysis are as follows: (a) $5.27 \mu\text{m}^{-2}$, (b) $3.39 \mu\text{m}^{-2}$, (c) $3.50 \mu\text{m}^{-2}$, (d) $4.57 \mu\text{m}^{-2}$, (e) $17.69 \mu\text{m}^{-2}$, and (f) $4.56 \mu\text{m}^{-2}$. Micrograph dimensions: $10 \mu\text{m} \times 7 \mu\text{m}$.

For compositions with high MoO₃ (≥ 7 mol%), particles also appeared to become more uniformly distributed with the range of PS becoming smaller by $\sim 40 - 75$ nm following irradiation. For fluences greater than 8×10^{13} ions/cm², BSE imaging also revealed the distortion of some originally spherical particles to those with oblong geometry, as Figure 2 indicates. These distortions could be attributed to surface roughness in these specific specimens, or to defect-

associated changes within crystal clusters along the crystal to glass interface. A tertiary option would be a relaxation phenomena at the surface that alters the viscosity of the surrounding amorphous network thereby influencing radiation-induced crystallization kinetics.

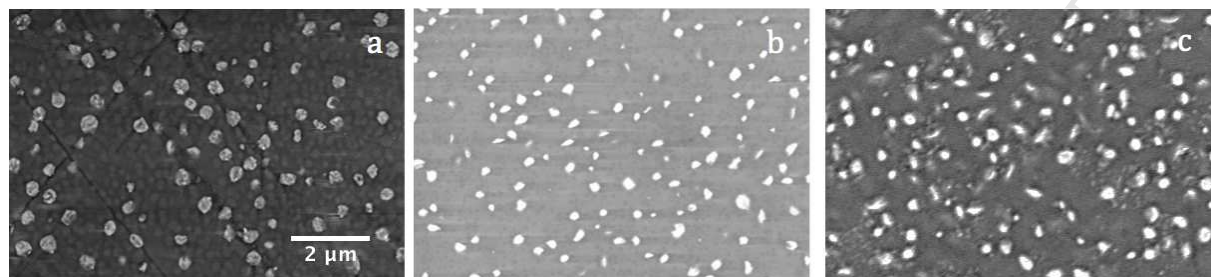


Figure 2. BSE images of CN10 at (a) pristine conditions, and following Xe-irradiation with fluences of (b) 8×10^{13} , and (c) 1.8×10^{14} ions/cm². The particle densities determined by image analysis are as follows: (a) $1.80 \mu\text{m}^{-2}$, (b) $2.39 \mu\text{m}^{-2}$, and (c) $2.24 \mu\text{m}^{-2}$. Micrograph dimensions: $10 \mu\text{m} \times 7 \mu\text{m}$.

Compositionally, there are several changes induced by Xe-irradiation, as Figure 3 illustrates. The results suggest migration of ionic species between the sample bulk and the surface. At low doses, an increase in the amount of Mo, Ca and Na is initially observed at the surface, followed by diffusion of Ca and Na atoms towards the bulk. This is represented by an increase in the [Si]/[Ca] and [Si]/[Na] ratios. As the BSE analysis depth is roughly $\sim 1 \mu\text{m}$, migration towards the “bulk” may still fall within the $\sim 12 \mu\text{m}$ irradiation zone.

This flux of ionic species could indicate ionization-induced migration and clustering of ions in which motion is driven by the added energy to the system, or by migration in a liquid phase following the creation of a thermal spike. Under the first process, it is assumed that a minimum fluence is required to exceed the activation barrier for motion. Furthermore, the rate of migration is different for each species owing to the size and charge of each respective element, hence why [Mo]/[Ca] changes. This difference subsequently results in a maximum [Mo] at the surface for

fluences $\leq 4 \times 10^{13}$ ions/cm², after which Mo ions also diffuse towards the bulk. The inflection points observed for the trends in Figure 3 indicate a critical dose at which Ca atoms that initially moved away from the surface re-precipitate at higher fluences. A similar trend is also found for Na atoms in the amorphous phase, but the rate of change is larger for this more mobile alkali ion.

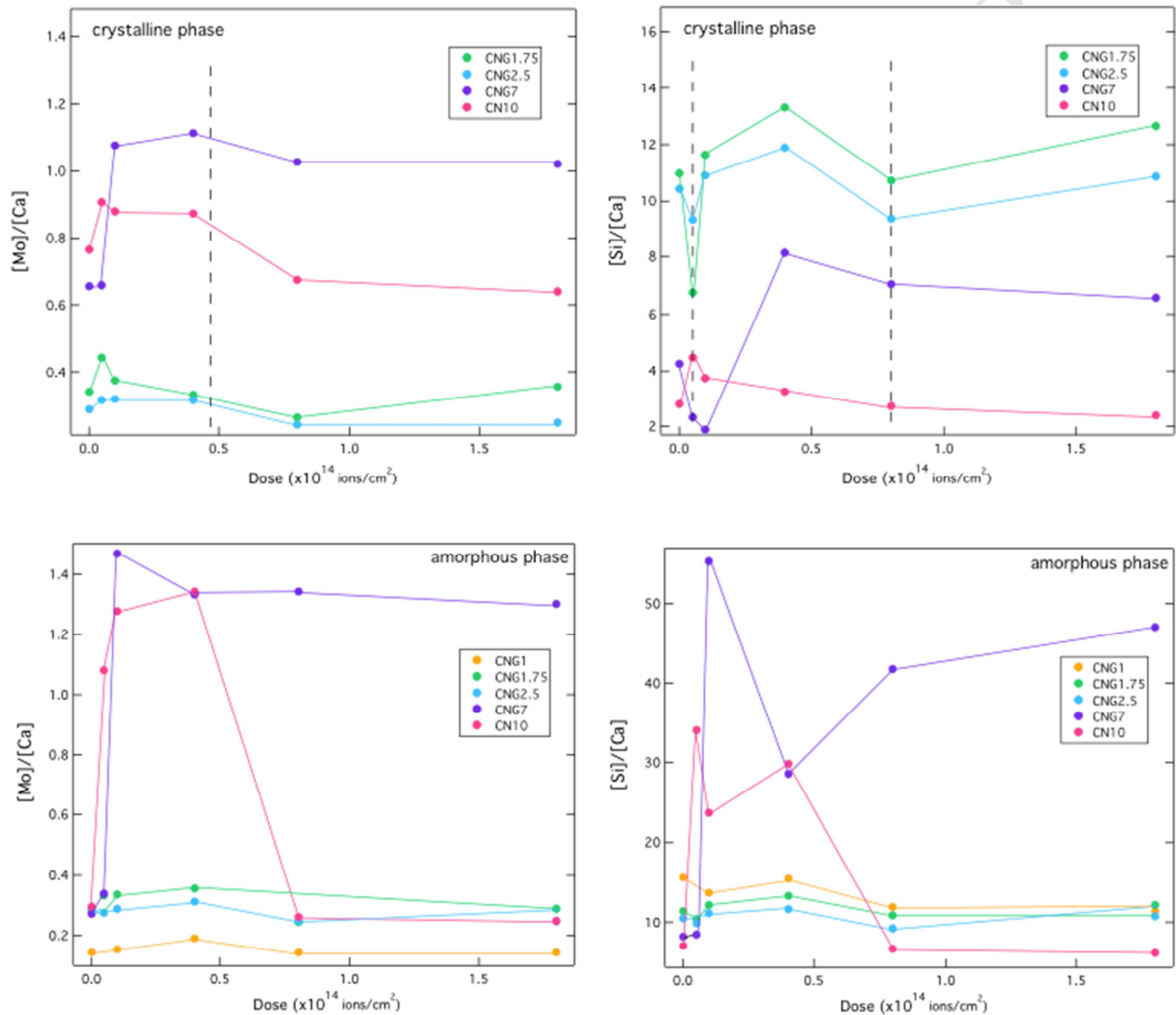


Figure 3. [Mo]/[Ca] and [Ca]/[Si] ratios for Mo-bearing glasses and GCs following Xe-irradiation with fluences between 5×10^{12} to 1.8×10^{14} ions/cm². Although not shown in the plots, Na ions follow a similar trend to Ca ions, but with larger magnitudes of change observed owing to the greater mobility of the ion. For the given plots, a saturation in modifications can be

observed around 8×10^{13} ions/cm². Note that crystalline measurements in low-Mo bearing samples also measure the surrounding amorphous area, hence why there is a higher [Si] and a lower [Mo]/[Ca] than would be expected. The relative trends with respect to dose are primarily of interest as opposed to the absolute values. Statistical error for calculated average ratios is < 1% (smaller than data points).

This re-precipitation is also true for Mo migration, but the rate of change is slower, and the magnitude of change smaller. At doses $\geq 8 \times 10^{13}$ ions/cm², a stabilization in composition is observed. These results suggest that surface-to-bulk diffusion and re-precipitation reach an equilibrium state, or that diffusion pathways become hindered, thus making ions less mobile within this small volume near the surface. This is not to say that the trends observed by EDS planar analysis are true throughout the whole irradiation zone, but they may be indicative of some of the processes occurring within this damaged volume.

These trends are evident for low Mo-bearing samples, but the induced alteration in high Mo-bearing GCs are much more erratic with a larger magnitude of change observed. For starters, there is a much larger decrease in [Ca] and [Na] within the amorphous phase following initial irradiation. In some cases, [Mo]/[Ca] of the amorphous phase also exceeds one following initial irradiation. This result could indicate a change in composition of the local amorphous network surrounding particles owing to a scattering of crystal constituents, or it could be influenced by measurements that included subsurface particles, which were partially identifiable by BSE imaging. Alternatively, it could imply the formation of defects or voids within crystals that released Ca atoms, which subsequently migrate rapidly away from the surface. For doses $\geq 4 \times 10^{13}$ ions/cm², trends imply some dissolution of Mo complexes from the surface towards the

bulk. In CN10, this is likely accompanied by some re-precipitation of Ca and Na atoms, hence why ratios return to values similar to those found at pristine conditions.

A general mechanism of surface-to-bulk migration is assumed for all compositions as the [Mo]/[Ca] trends with respect to fluence are similar for measurements of different compositions, and in both the crystalline and amorphous phase of each composition. These trends are also evident for the [Mo]/[Na] ratios within the amorphous phase. It is therefore predicted that some initial surface-to-bulk migration of CaMo-species and Na ions takes place, followed by re-precipitation at higher doses. The initial surface depletion of cations is presumed to be associated with a charge driven migration of ions into the bulk. This response has previously been seen for Na⁺ ions following irradiation [28,32]. It is predicted to occur from electric field-assisted diffusion, along with a kinetic energy transfer from the incoming ions.

The initial migration of Ca and Na atoms at low Xe fluences is particularly pronounced in the amorphous phase of high Mo-bearing GCs (CNG7 and CN10). This result indicates the network-modifying role of these cations when dispersed in the amorphous phase, as opposed to acting as a network former, hence why migration is easily enabled. The formation of larger particles in high Mo-bearing GC compositions also appears to have enabled easier migration of Ca ions, hence why a larger change in magnitude is observed. It suggests that radiation can more easily affect Ca in the crystalline phase, as opposed to Ca in the amorphous phase. While the cause of these compositionally dependent alterations is not clear from these results alone, the general ratio patterns with respect to dose suggest a saturation in compositional changes in both crystalline precipitates and the amorphous phase within this planar surface for doses $\geq 8 \times 10^{13}$ ions/cm² (see Figure 3). This effect may vary as a function of depth owing to changes in the ion stopping

power, with current results only providing effects of electronic interactions at the surface where a large thermal spike is expected.

3.3 Changes to crystallinity following irradiation

XRD confirmed the existence of a single tetragonal scheelite-type powellite (CaMoO_4) structure with a $I4_1/a$ space-group following irradiation. This indicates that no cationic substitution or formation of Na_2MoO_4 took place (see Supplementary information A1.2). This result implies that molybdenum can be trapped in a radiation-resistant powellite structure without converting to yellow phase constituents in simplified systems during simulated long-term storage.

There was however a marginal whole CaMoO_4 pattern amplitude dampening indicative of partial amorphization or increased disorder (see Supplementary Information for XRD spectra). There were also observed changes to the CaMoO_4 structure and size following Xe-irradiation. This was determined by whole pattern Rietveld refinements using Topas v4.1 [30] and the crystal structure for powellite (22351-ICSD), where peak broadening was fit with a single Scherrer CS parameter and peak position was used to determine the tetragonal unit cell parameters. The results of this analysis are summarized in Table 2.

Table 2. CS in diameter and cell parameter of powellite in Xe-irradiated GCs.

Sample	Fluence (ions/cm ²)	CS (nm)	a (Å)	c (Å)
CNG1.75	0	51.27 (\pm 2.26)	5.2289 (\pm 0.0011)	11.4606 (\pm 0.0034)
	5×10^{12}	47.24 (\pm 1.61)	5.2332 (\pm 0.0005)	11.4603 (\pm 0.0023)
	1×10^{13}	38.49 (\pm 1.31)	5.2328 (\pm 0.0011)	11.4678 (\pm 0.0036)
	4×10^{13}	50.48 (\pm 1.66)	5.2341 (\pm 0.0008)	11.4625 (\pm 0.0025)
	8×10^{13}	50.15 (\pm 1.99)	5.2313 (\pm 0.0009)	11.4606 (\pm 0.0028)

	1.8×10^{13}	45.89 (± 1.30)	5.2310 (± 0.0007)	11.4610 (± 0.0023)
CNG2.5	0	55.09 (± 2.08)	5.2280 (± 0.0080)	11.4593 (± 0.0025)
	5×10^{12}	59.85 (± 2.52)	5.2311 (± 0.0080)	11.4695 (± 0.0027)
	1×10^{13}	39.77 (± 2.51)	5.2327 (± 0.0019)	11.4576 (± 0.0066)
	4×10^{13}	47.46 (± 2.44)	5.2336 (± 0.0013)	11.4658 (± 0.0038)
	8×10^{13}	42.38 (± 5.38)	5.2275 (± 0.0020)	11.4548 (± 0.0081)
	1.8×10^{13}	50.90 (± 5.23)	5.2292 (± 0.0017)	11.4614 (± 0.0059)
CNG7	0	143.38 (± 2.54)	5.2265 (± 0.0001)	11.4558 (± 0.0003)
	5×10^{12}	175.14 (± 7.42)	5.2332 (± 0.0002)	11.4688 (± 0.0008)
	1×10^{13}	53.05 (± 0.91)	5.2330 (± 0.0004)	11.4611 (± 0.0012)
	4×10^{13}	49.11 (± 0.74)	5.2302 (± 0.0004)	11.4553 (± 0.0012)
	8×10^{13}	52.24 (± 0.91)	5.2323 (± 0.0004)	11.4585 (± 0.0012)
	1.8×10^{13}	56.27 (± 0.91)	5.2320 (± 0.0003)	11.4586 (± 0.0009)
CN10	0	125.24 (± 1.94)	5.2264 (± 0.0001)	11.4554 (± 0.0030)
	5×10^{12}	61.93 (± 1.90)	5.2316 (± 0.0003)	11.4582 (± 0.0014)
	1×10^{13}	45.23 (± 0.76)	5.2336 (± 0.0004)	11.4613 (± 0.0015)
	4×10^{13}	48.29 (± 0.83)	5.2325 (± 0.0004)	11.4577 (± 0.0013)
	8×10^{13}	50.12 (± 0.83)	5.2332 (± 0.0005)	11.4604 (± 0.0016)
	1.8×10^{13}	51.20 (± 0.87)	5.2334 (± 0.0004)	11.4613 (± 0.0011)

For all GCs, CS decreases and the cell parameters increase from pristine conditions to the highest fluence of 1.8×10^{14} ions/cm², although a non-linear trend is observed with respect to dose. In general, CS was observed to exponentially decay in most compositions, while the cell parameters initially increased and then decreased before reaching a plateau in modifications as the graphical representations in Figures 4 & 5 illustrate.

In CNG7 and CNG2.5, an initial small increase in CS was observed following irradiation with 5×10^{12} ions/cm², before decreasing and saturating for doses between 1×10^{13} to 1.8×10^{14} ions/cm². In contrast, CNG1.75 and CN10 showed an immediate decrease in CS following irradiation, followed by a similar saturation for doses between 1×10^{13} to 1.8×10^{14} ions/cm². Within this saturation regime a small growth in CS is observed, but this can still be considered an equilibrium state of crystallinity given that the differences observed are relatively small within a significantly large fluence range, and that they generally fall within uncertainty. The changes do however indicate that small defects are still forming in and around crystallites with increasing fluence, but that some sort of competing processes may be limiting their formation or stability.

For high Mo-bearing GCs, the CS and cell parameter trends with respect to fluence are easy to identify (see Figure 4). Both the *a* and *c* cell parameters are observed to first increase with initial radiation before decreasing at medium fluences (~ 1 to 4×10^{13} ions/cm²). They then increase again before saturating at higher fluences ($\geq 8 \times 10^{13}$ ions/cm²). The uniform trends between the *a* and *c* cell parameters as a function of fluence indicate that the processes of expansion and contraction are directionally uniform. However, the magnitude of change is always larger in the *c*-direction.

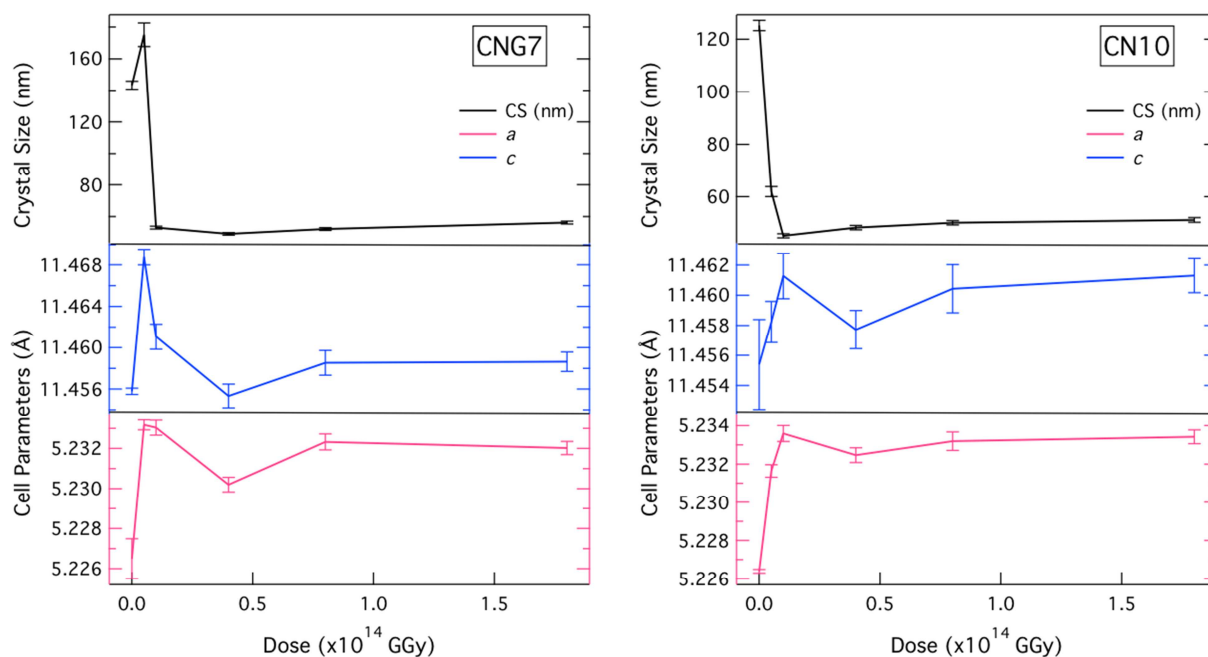


Figure 4. Changes to powellite CS and cell parameters following Xe-irradiation with fluences between 5×10^{12} to 1.8×10^{14} ions/cm² in high Mo-bearing GCs (with [MoO₃] ≥ 7 mol%). Top to bottom: CS, *c* cell parameter, and *a* cell parameter.

In contrast, the trends observed for low Mo-bearing samples are more difficult to discern owing to the large margin of error, as Figure 5 illustrates. A similar trend for the cell parameters with respect to dose is observed, although this is less notable for the *a* cell parameter where it first increases and then gradually decreases to a saturation point. It is worth noting that in both cases the observed changes could fall within error. It is, however, interesting to identify that both the cell parameters and CS approach pristine conditions following irradiation with 1.8×10^{14} ions/cm². Therefore, it can be assumed that most structural changes to the powellite unit cell created by initial irradiation were recovered with increasing dose in these low Mo-bearing GCs.

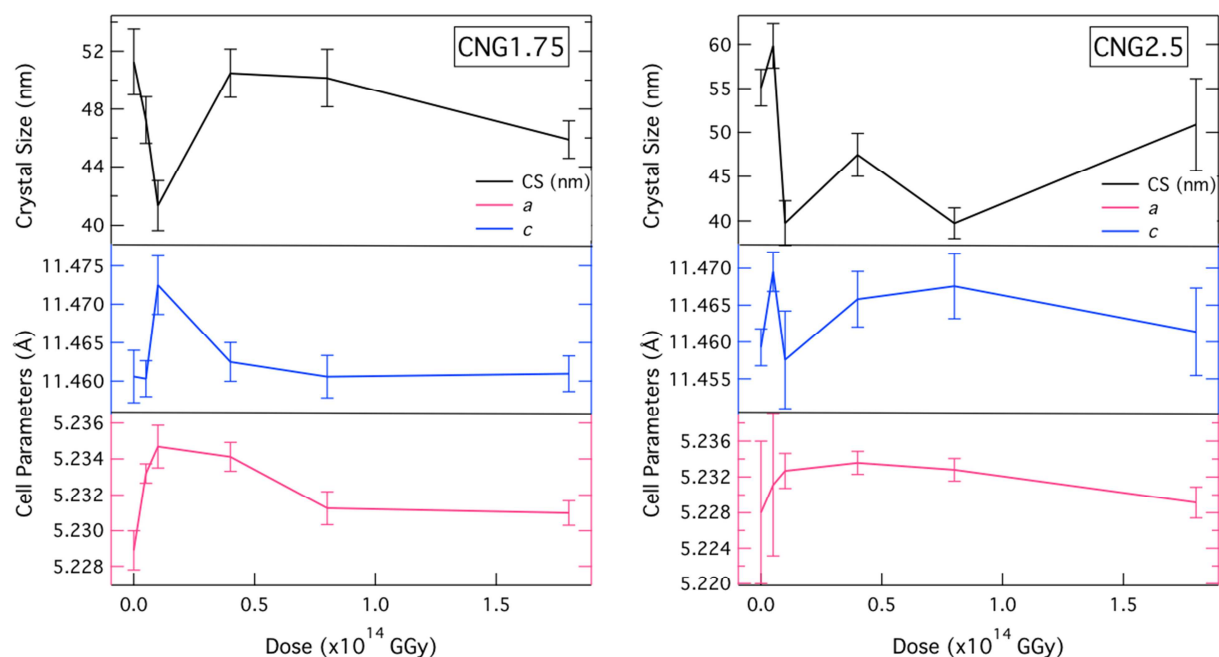


Figure 5. Changes to powellite CS and cell parameters following Xe-irradiation with fluences between 5×10^{12} to 1.8×10^{14} ions/cm² in low Mo-bearing GCs (with [MoO₃] \leq 2.5 mol%). Top to bottom: CS, c cell parameter, and a cell parameter.

3.4 Changes to bonding following irradiation

Raman spectroscopy was used to determine bonding changes in both the amorphous and crystalline phases. Within the powellite phase there are six relevant internal modes for MoO₄²⁻ in crystalline CaMoO₄. The vibrations relate to symmetric elongation of the molybdenum tetrahedra $\nu_1(A_g)$ 878 cm⁻¹; asymmetrical translation $\nu_3(B_g)$ 848 cm⁻¹ and bridging $\nu_3(E_g)$ 795 cm⁻¹ of molybdate chains; asymmetric O–Mo–O bending modes $\nu_4(E_g)$ 405 cm⁻¹ and $\nu_4(B_g)$ 393 cm⁻¹; and symmetric bending $\nu_2(A_g+B_g)$ 330 cm⁻¹. Additionally there are three external modes $\nu_{\text{def}}(A_g)$ at \square 206 cm⁻¹, 188 cm⁻¹, and 141 cm⁻¹ assigned to translational modes of Ca–O and MoO₄ [33–36]. Following irradiation all of these internal and external MoO₄²⁻ modes are still visible indicating rigidity of the molybdenum tetrahedron, but the bands experience peak shifts

and broadening, which thus implies increased structural disorder (see Figure 6 and Supplementary Information A1.3 for additional spectra).

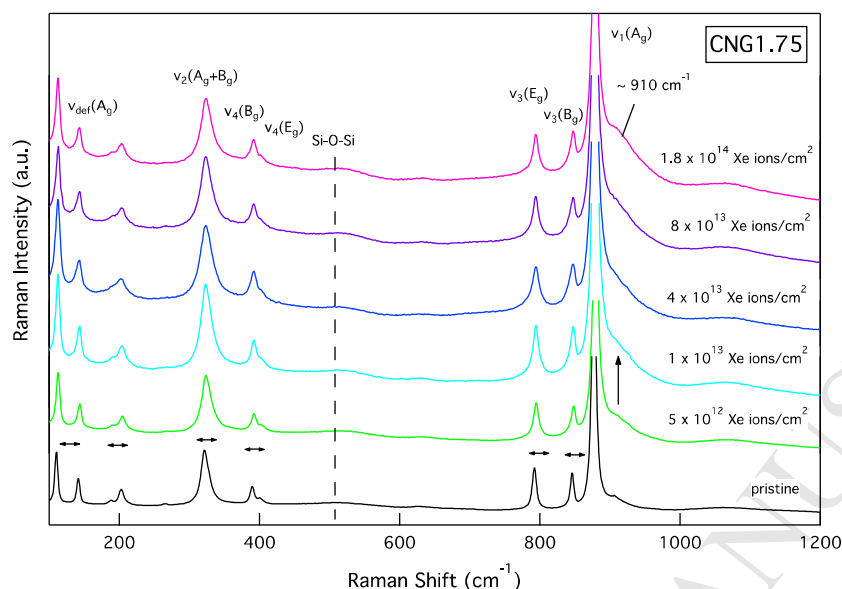


Figure 6. Raman spectra of irradiated CNG1.75. Fluences and bands of interest have been labeled. A general broadening of internal MoO_4^{2-} modes, along with growth of the band associated with dissolved molybdenum in the amorphous network ($\sim 910 \text{ cm}^{-1}$) is observed as dose increases.

In all GCs, internal MoO_4^{2-} modes experience a peak shift to lower wavenumbers, together with peak broadening of approximately $2 - 3 \text{ cm}^{-1}$. This is quantified for the symmetric elongation mode $\nu_1(\text{A}_g)$ in Figure 7. Radiation is initially observed to induce a peak shift of $1.2 - 2.0 \text{ cm}^{-1}$ to higher wavenumbers following a dose of $5 \times 10^{12} \text{ ions/cm}^2$, after which the peak approaches its position at pristine conditions (at lower wavenumbers) through an exponential decay. Correspondingly, the greatest change in peak broadening was observed at the lowest fluence, but the peak full-width half maximum (fwhm) continues to grow with increasing fluence. The continual increase in peak broadening is indicative of an increased disruption in long-range ordering.

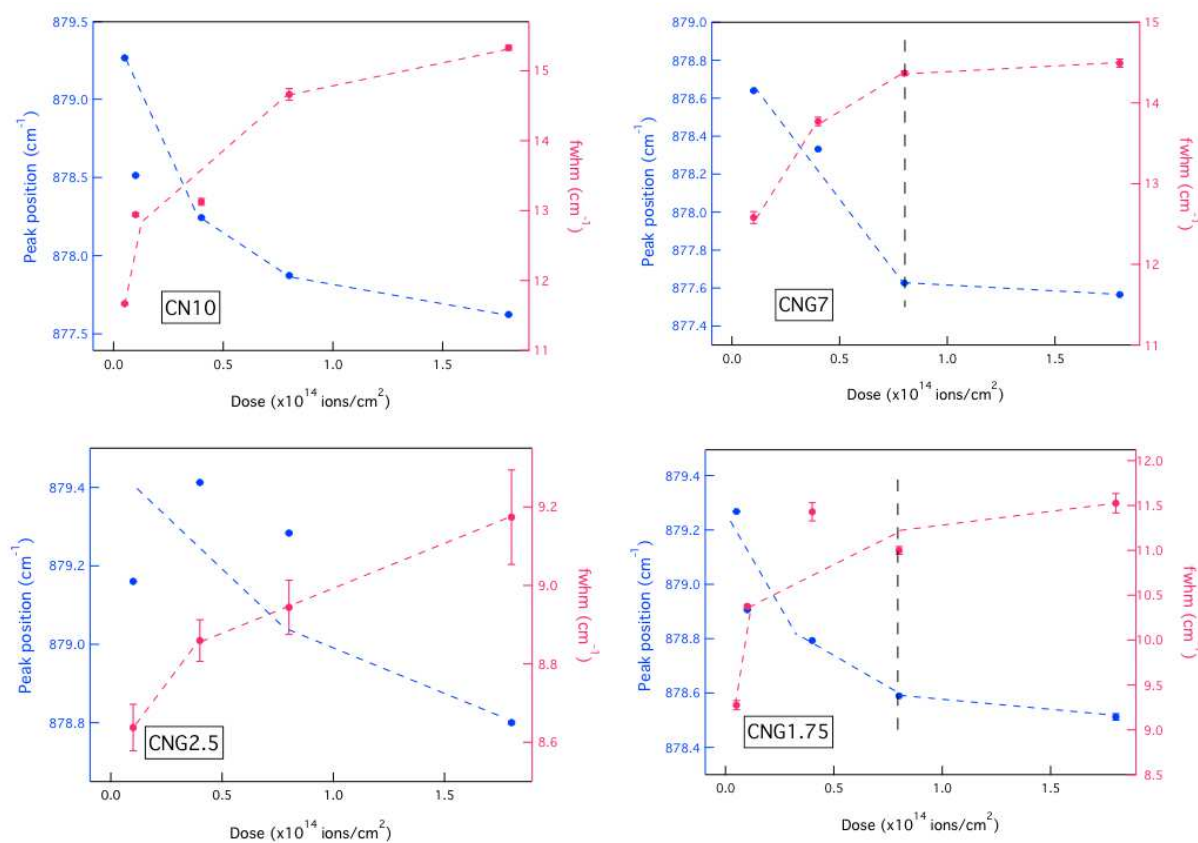


Figure 7. Changes to the position and broadening of the internal MoO_4^{2-} Raman mode for crystalline powellite assigned to symmetric elongation $\nu_1(A_g)$ in Xe-irradiated GCs. Pristine data points are not given in these plots, but the relative results are described in the text (pristine peak position between $877.5 - 877.1 \text{ cm}^{-1}$, and fwhm $8.6 - 7.7 \text{ cm}^{-1}$ for high – low Mo-bearing samples). Dashed lines represent plateaueed growth and decay, but they deviate from data points on several occasions.

For most of the samples, the rate of change in both the peak position and fwhm decreased significantly around a fluence of $8 \times 10^{13} \text{ ions/cm}^2$. A plateau in modification was recognizable around this fluence for CNG7, with a similar pattern evident for CN10 and CNG1.75 despite some fluctuations. While the same general trend can be seen for CNG2.5, there was a greater scatter in the data, introducing some uncertainty with regards to the radiation response of this

composition. The changes to peak position appeared to be delayed, which suggests that the fictive temperature of this system following synthesis was different than the other GCs despite a uniform methodology. Discrepancies arising from this hypothesis of the initial state of relaxation have been observed for similar compositions to CNG2.5 when subjected to β -irradiation [14,37].

While the greatest change to peak broadening of internal MoO_4^{2-} modes was observed at the lowest fluence, the opposite trend was found for external modes. In most compositions the external mode at $\sim 188 \text{ cm}^{-1}$ reached a maximum with respect to peak broadening at $8 \times 10^{13} \text{ ions/cm}^2$, after which the peak fwhm was similar to those found for samples irradiated with 1 to $4 \times 10^{13} \text{ ions/cm}^2$. The collective results indicate that irradiation first impacts the bonds within MoO_4^{2-} tetrahedra, before altering the bonds within crystal chains. They also indicate that there was some recovery of defects within MoO_4^{2-} tetrahedra and between tetrahedra (external modes), hence why the rate of change decreases in Figure 7 and a saturation in peak broadening and peak position shifts are observed for fluences $\geq 8 \times 10^{13} \text{ ions/cm}^2$. This implies that there are competing processes that cause and anneal damage, which is why a plateau in changes is observed. This theory can be similarly applied to CS results in Figures 4 & 5 that similarly display an equilibrium state. However, it is important to outline that this equilibrium state still contains many defects, as compared to the pristine structure.

In GCs with $[\text{MoO}_3] \leq 2.5 \text{ mol\%}$, Raman spectra also show growth of an amorphous band at $\sim 910 \text{ cm}^{-1}$ that is associated with symmetric stretching vibrations of MoO_4^{2-} tetrahedral units located in amorphous systems [38] with increasing Xe-irradiation. The trends in Figure 8 indicate that the area of this peak continues to increase until reaching saturation for fluences between 4 to $8 \times 10^{13} \text{ ions/cm}^2$, which coincides with a $\sim 43\%$ increase in the area of this band. This result suggests that some crystallites may initially be amorphizing at low doses, or that

increasing disorder is significantly effecting the stacking of unit cells, and therefore causing the isolation of some MoO_4^{2-} tetrahedra. However, this process appears to be limited given that a saturation period appears at higher doses, further indicative of competing damage creation and recovery processes following radiation.

Given that the Raman spot size of $\sim 1 \mu\text{m}$ is larger than particles in this low $[\text{MoO}_3]$ range, measurements were randomly made and likely incorporated both crystalline particles and the surrounding amorphous phase. In order to ensure that trends were accurate for each sample multiple measurements were made, where the Raman spectra appeared the same for each measurement. Therefore, growth of the band at $\sim 910 \text{ cm}^{-1}$ is representative of changes within the bulk surface (both the amorphous and crystalline phases as a collective).

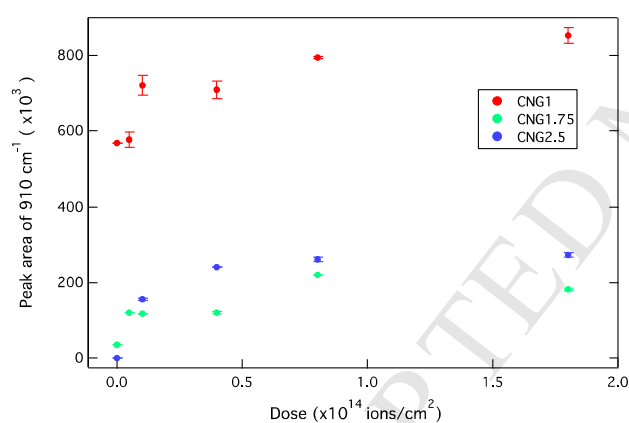


Figure 8. Area evolution of the Raman peak at $\sim 910 \text{ cm}^{-1}$ associated with MoO_4^{2-} tetrahedra dissolved in an amorphous network for samples CNG1 (glass), CNG1.75 and CNG2.5 (GCs) following Xe-irradiation.

In addition to the changes within the molybdenum environment, the amorphous network in both GCs and pure glasses also exhibited several changes following irradiation. The glass CNG1 similarly exhibited growth of the band at $\sim 910 \text{ cm}^{-1}$, before a plateau in modifications could be detected for fluences greater than $4 \times 10^{13} \text{ ions/cm}^2$. This result implies that there may have been

very small crystallites existing in CNG1 beyond SEM detection limits that dissolved following irradiation. Or it could be indicative of a reorganization of clustered MoO_4^{2-} tetrahedra within the amorphous phase that caused isolation of many MoO_4^{2-} units.

Previous works have indicated that although molybdenum groups are interspersed in a homogeneous glass, molybdenum is still tetrahedrally coordinated as MoO_4^{2-} and exhibits some general order with local Ca^{2+} ions. Therefore, molybdenum that does not crystallize remains trapped in an amorphous form of $\text{Ca}_x[\text{MoO}_4]_y$, which produces similar vibrational bands to the crystalline phase of powellite [14,39,40]. Using this theory, growth of the band at $\sim 910 \text{ cm}^{-1}$ could indeed be isolation of MoO_4^{2-} units within the amorphous phase from an initial clustered arrangement.

CNG1, in addition to CNO, also exhibited several characteristic bands for the borosilicate network (see Supplementary information A1.3 for spectra). These include a broad band around $\sim 450 \text{ cm}^{-1}$ attributed to Si-O-Si and Si-O-B bending and rocking [19,41], a band at $\sim 633 \text{ cm}^{-1}$ assigned to Si-O-B vibrations in danburite-like $\text{B}_2\text{O}_7\text{-Si}_2\text{O}$ groups [19,42], a low intensity broad band at $\sim 1445 \text{ cm}^{-1}$ assigned to B-O⁻ bond elongation in metaborate chains and rings [19], a narrow band around $\sim 807 \text{ cm}^{-1}$ assigned to the symmetric vibrations of 6-membered boroxyl rings of BO_3 -triangles [43–45] with a broader band at $\sim 800 \text{ cm}^{-1}$ assigned to O-Si-O stretching [46], as well as bands between $\sim 700 - 800 \text{ cm}^{-1}$ attributed to the vibrations of rings containing one or two tetrahedrally coordinated boron centers [19,45,47], and Si-O stretching vibrational modes for Q^n entities that represent SiO_4 units with n bridging oxygen between $845 - 1256 \text{ cm}^{-1}$. While the spectral shape of these amorphous bands remained similar, growth in the area of the band at $\sim 1445 \text{ cm}^{-1}$, together with dampening of the band attributed to danburite-like rings occurred in all glasses. In compositions without molybdenum there was also dampening of the

characteristic band assigned to metaborates ($\sim 703 \text{ cm}^{-1}$), while a growth in the area of the band at $\sim 910 \text{ cm}^{-1}$ was found for CNG1 (glass with molybdenum).

Irradiation also caused an emergence of the D^2 ($\sim 606 \text{ cm}^{-1}$) defect band, which is assigned to the breathing of 3-membered SiO_4 rings [48]. This occurred alongside a shift of the Si-O-Si band to higher wavenumbers, which indicates smaller inter-tetrahedral angles. This shift can be caused by the formation of smaller rings, or by the distortion of existing ring structures. These changes can also be observed to occur following irradiation in low Mo-bearing GCs. Therefore, the results suggest the cleavage and reformation of smaller borosilicate rings that may be aiding in the increased solubility of MoO_4^{2-} tetrahedra. This process is associated with de-mixing of the borosilicate network, and possible glass-in-glass phase separation.

4.0 Discussion

In this study, we were primarily testing the durability of CaMoO_4 embedded in a borosilicate matrix against amorphization or cationic substitution following irradiation that simulated the damage created by α -decay events consistent with storage over ~ 1000 years. It was also used to assess whether the added energy from ion bombardment could cause either precipitation of additional crystalline phases, or the amorphization of pre-existing separated phases. The behavior of the residual glass matrix was also of interest, to see if it responded to radiation in the same manner with and without interspersed molybdate crystallites.

The results indicate that Xe-irradiation caused changes to both the amorphous and crystalline phase, but that these changes appeared to saturate in the bulk for doses $\geq 8 \times 10^{13} \text{ ions/cm}^2$. This is an important observation, which indicates that while the mechanisms of alteration may be continuous, an average damage structure can be predicted for long-term assessment.

4.1 Changes to the amorphous phase

The initial aims of this study were to identify if long-term radiation damage would: (i) induce phase separation in homogenous systems, (ii) propagate existing phase separation, or (iii) cause the amorphization of crystallites through local annealing. Using the results from the amorphous sample CNG1 it can be determined that irradiation did not cause the precipitation of any molybdates at the surface, which would have created diffraction peaks and Raman vibrations if it occurred. In fact, irradiation was observed to increase the disorder of MoO_4^{2-} tetrahedral units. This is exemplified by a broadening of internal MoO_4^{2-} Raman vibrations, along with growth of the band at $\sim 910 \text{ cm}^{-1}$ attributed to dissolved monomers in the amorphous network. This increase in disorder is combined with changes to the ring structures within the borosilicate framework, which shows the formation of smaller or distorted rings with smaller intertetrahedral angles following irradiation. This latter result has also been observed to occur in glasses without molybdenum [5,19,26,28], which suggests that the residual amorphous network behaves in a similar manner with and without embedded CaMoO_4 crystallites.

4.2 Radiation-induced amorphization

While precipitation of crystallites in glasses was easy to assess, changes to crystallization in GCs was more complex. Growth of the Raman band at $\sim 910 \text{ cm}^{-1}$ and a small uniform dampening of XRD spectra (see Supplementary Information A1.2) indicate possible amorphization of small CaMoO_4 crystallites, or at the very least local damage that causes a reduction in the average crystal quality in GCs following irradiation. This statement is supported by EDS analysis, which suggests that Ca atoms move from crystal particles towards the amorphous matrix, in addition to some Mo dissolving into the glassy matrix or towards the bulk for doses exceeding $5 \times 10^{12} \text{ ions/cm}^2$. However, the EDS results presented here only represent changes at the surface, while XRD and Raman results probe a much larger volume.

Electric field induced diffusion has been previously observed to occur in irradiated alkali-containing glasses, which would subsequently cause the concentration of alkalis and alkali earths at the surface to change following ion interactions [49,50]. Therefore, the migration of Ca and Na ions theorized to occur in this study is very possible. The deposited energy from Xe-irradiation could also be contributing to a change in the void population, which could thus affect diffusion processes following irradiation.

While radiation-induced amorphization of powellite crystals has not been previously observed [14,15,31,51], it has been noted to occur in other irradiated ceramics [21,52]. In these systems, partial amorphization was predicted to occur following radiation-induced atomic displacements and the formation of isolated defects. This process of amorphization is theoretically different from temperature-induced amorphization where atoms are completely random in configuration. In radiation-induced processes, amorphization occurs heterogeneously when a critical defect population is reached [21]. As a result, these defects can often be thermally annealed at temperatures lower than the crystallization temperature (T_C).

Alternatively, another theory indicates that amorphization could be proceeding through thermal-like events. *Naguib and Kelly* predicted that amorphization of non-metallic structures could occur following SHI-irradiation for doses between 10^{13} to 10^{17} ions/cm². This hypothesis was based on a physical model involving thermal spikes with a criticality condition for amorphization of $\frac{T_C}{T_m} > 0.3$ [53]. Given that $\frac{T_C}{T_m} \rightarrow 0.8$ for synthetic powellite, and that some of the fluences in this study fall within the predicted amorphization range, it is possible that this process of amorphization through thermal spikes does take place.

If amorphization is occurring in these GCs, there are several possible mechanisms. Previous studies have indicated that amorphization from ion irradiation can occur through direct-impact

within an ion track, from overlapping collision cascades that create a high defect population, or through a nucleation and growth process in which a small amorphous nuclei initiates the transformation [20,54,55]. A combination of any of these processes could also be occurring, as the type of mechanism is generally dependent on the composition under irradiation. In general, direct-impact processes would have a logarithmic impact on amorphization with respect to dose, while overlapping collision cascades (or ion tracks) would have a sigmoidal relationship to dose. In contrast, nucleation and growth would require a significant incubation period that necessitates the accumulation of defects in a given area, and thus has a more exponential relationship with dose.

Given that a saturation in [Mo] and the Raman band associated with dissolved MoO_4^{2-} in the amorphous network is found within the fluence range achieved in this study, it is predicted that any amorphization of powellite crystals occurs through direct-impact collisions or from overlapping cascades. As Xe ions primarily replicate electronic interactions, it can further be predicted that ion tracks, as opposed to collision cascades, are the driving force of amorphization in these GCs.

It is assumed that where amorphization did occur, only small crystallites dispersed in the amorphous network were affected, as opposed to those forming larger particles. Furthermore, it is predicted that a saturation in this process arises due to parallel diffusion and re-precipitation of CaMo-rich particles at the surface with increasing fluence, as EDS analysis implies. It is hypothesized that this process of diffusion is related to the formation and stability of defect-enabled pathways, and to an increase in the kinetic energy within the system from temperature-like effects of overlapping ion tracks that would subsequently initiate ionic movement.

Therefore, it is predicted that modifications to powellite crystals involve minor defect-assisted amorphization and diffusion driven re-precipitation and particle growth at high doses.

4.3 Alterations to crystalline phase

Following irradiation powellite was the only crystalline phase detected. The more water-soluble Na_2MoO_4 phase was not produced, nor was a $\text{Gd}_{0.5}\text{Na}_{0.5}\text{CaMoO}_4$ phase. If Na^+ or Na-Gd substitution of Ca^{2+} ions took place, refinement of the calcium site occupancy would have detected markers for the new complexes, as has previously been used for rare-earth substitution where the covalent size of elements differs substantially [15,56].

As discussed in the previous section, heterogeneous amorphization of some powellite crystallites may be taking place in low Mo-bearing GCs. That being said, this is likely only a minor process, as the particle density of samples did not vary significantly following irradiation, according to SEM imaging. Furthermore, only a minor dampening of diffraction peaks was observed, indicative of a lasting population of powellite. Yet, the results suggest that the individual crystallites experienced structural changes following irradiation.

XRD results suggest a mechanism in which isolated defects rapidly accumulate within the lattice structure of crystallites following initial ion bombardment. This accumulation caused an expansion of the unit cell, and an initial expansion in CS, followed by a reduction. This reduction in CS is caused by a disruption in the coherence length, which occurs when crystals become significantly disordered through atomic displacements, line or plane defects. Therefore, it is deduced that initial radiation replicates thermal like expansion or CS growth through the annealing of defects created during synthesis, while accumulated radiation damage causes irreparable damage to the order within crystals. The degree of damage for fluences greater than 1×10^{13} ions/cm² is however limited by recovery processes more prominent at lower fluences,

which is why a saturation is observed as opposed to a continual CS decrease leading to full amorphization.

In terms of the unit cell expansion, a similar trend has been previously observed to occur following Ar-irradiation of powellite single crystals [51], with thermal expansion similarly occurring for single crystals subjected to high temperature [57,58]. Therefore the trends for the tetragonal powellite unit cell parameters following irradiation are logical, but little to no data exists for CS alteration following irradiation.

When these GCs are initially irradiated, the rate and magnitude of change for both CS and the a and c cell parameters are found to be dependent on composition and the relative structure of the residual amorphous matrix. Larger particles in compositions with $[\text{MoO}_3] \geq 7$ mol% show the clearest shifts in cell parameters with respect to dose, while those with a higher concentration of MoO_4^{2-} units dissolved in the matrix show relatively smaller changes. This is because CS and PS were very small to begin with in compositions with $[\text{MoO}_3] < 7$ mol%, and therefore less susceptible to ion interactions on a probability basis.

As Xe-irradiation increases, the unit cell generally contracts again, as accumulated defects cannot be indefinitely supported and must be relieved through transformations, such as dislocations [59]. This process would enable the observed relaxation of the unit cell. Alternatively, a contraction of the unit cell could also be caused by a localized pressure-induced stress [60]. In this scenario, the accumulation of defect-created vacancies within crystal chains could exert a small force on adjacent unit cells, thus resulting in unit cell contraction. This process has been previously predicted to occur in apatites following α -decay [20].

Thermal annealing of existing defects through overlapping ion tracks could also be contributing to the observed unit cell contraction of high Mo-bearing samples (see Figure 4). In

this case, thermal-like processes could enable relaxation of the unit cell by removing associated defects, versus causing thermal expansion. The cycle then repeats, but it is predicted that the defect population is being constantly controlled by ‘thermal’ annealing processes, as the density of overlapping ion tracks increases with increasing fluence. This is why a saturation in both CS and the cell parameters is detected for doses greater than 4×10^{13} ions/cm². This mechanism of alteration is predicted to occur in high Mo-bearing compositions with an original CS > 100 nm.

A similar interplay of processes causing unit cell expansion and contraction with increasing fluence is also assumed to occur in low Mo-bearing samples (see Figure 5). In these compositions, the formation of dislocations is however predicted to occur less frequently, and when it does, a much higher fluence is required to cause the same structural transformations. Therefore, the only mechanism of recovery against accumulated point defects in these compositions comes from overlapping ion tracks. The magnitude of change in CS for these low Mo-bearing samples is very small from pristine conditions to the maximum Xe fluence. This result implies that any modifications to the crystal structure within these compositions will be minor. Therefore, it can be assumed that the bulk of powellite crystals are fairly stable against Xe-irradiation, the exception being minor amorphization. Furthermore, EDS and Raman results indicate that any amorphization of small crystallites reaches a plateau in modifications around 4 to 8×10^{13} ions/cm². Therefore, this process is also limited and will not indefinitely continue to grow with increasing dose.

While several changes to the crystallinity of powellite are observed following irradiation, it can be concluded that Xe-irradiation did not induce the precipitation of additional molybdates, nor did it induce the substitution of the Na⁺ into powellite on an identifiable scale. This is proven by XRD and Raman results, which would have shown additional peaks if either transformation took

place. Furthermore, the identification of a saturation in modification implies that competing processes are limiting crystallite alteration. This equilibrium in crystallinity can therefore be used as a representation of the maximum modifications expected during long-term storage of nuclear waste in similar GCs.

4.4 Applicability and limitations of results

While these results represent an important initial discovery to a possible maximum damage state within these GCs, these results are true only for these simplified compositions when subjected to external SHI-irradiation. Results indicate that although modifications in both the amorphous and crystalline phase are small for the given doses and dose rates, they may vary with higher doses and slower dose rates typical for real processes, or integrated radiation types that replicate ballistic collisions as well as β -decay.

In this paper, a significant mechanism of defect-assisted Ca and Mo bulk-to-surface migration was observed by surface EDS analysis. This is likely a result of the high dose rate used and the associated charge of large impinging ions that can create an electric field gradient at the surface or a large thermal spike, as opposed to the final deposited energy. Therefore, in real internal decay processes, this type of charge-assisted migration may be less significant with internal radiation events proceeding in all directions, as opposed to ion bombardment perpendicular to the sample surface. Additionally, the crossings of ions tracks in real internal decay processes may enable some annealing of defects, which would subsequently further dampen defect-assisted migration. Although the migration of atoms is predicted to result primarily from the formation of structural defects, the kinetic energy deposited by higher-energy external radiation may also assist with atomic motion in these SHI-irradiation experiments.

In order to validate the use of SHI-irradiation in GC materials and to determine if these structural modifications caused by external irradiation are true for internal decay, doping GC compositions with α -emitters such as ^{244}Cm may be beneficial to understanding processes at slower dose rates. The use of additional analytical techniques that examine the cross section of SHI-irradiated samples as a function of depth may also prove useful to understanding how the mechanisms of radiation damage will vary with ion energy. This can also be used to isolate the effects of electronic interactions from those of ballistic nuclear events, which can be associated with self-healing and damage [22].

In addition to dose and dose rate effects of irradiation, composition must also be considered. In real nuclear waste materials, compositions will be much more complex, which can alter phase separation tendencies of the base glass, as well as migration of cationic species. However, the initial results suggest that the residual glass behaves in a similar manner with and without embedded CaMoO_4 particles. This implies that the crystalline phase may be stable with increasing additives, with the exception of rare-earth incorporation or cationic substitution. It further suggests that the majority of changes following an increase in composition complexity may occur within the amorphous phase, which is structurally suited for a range of ions.

Incorporation of Gd^{3+} into the CaMoO_4 structure as a Na-Gd complex was not detected in this paper, which implies that substitution of active minor actinides or lanthanides would not take place in radioactive systems. However, as only trace amounts were used in this study, incorporation of rare earths, which can act as actinide surrogates, could take place for concentrations exceeding 0.15 mol%. Therefore, it would be useful to increase the dopant amount in future investigations.

5.0 Conclusions

The aim of this work was to investigate the radiation resistance of new materials that could increase nuclear waste loading by trapping problematic molybdenum in a water-durable crystalline phase. In this study, several simplified borosilicate glasses and GCs containing powellite were irradiated with 92 MeV Xe ions to replicate the damage arising from α -decay events predicted to occur during long-term storage. The mechanisms of alteration were investigated using XRD, SEM imaging and quantitative analysis, as well as Raman spectroscopy. Together these techniques were able to describe changes to crystallinity, particle morphology, the relative composition of different phases, and any possible cationic substitution into powellite. The results indicate that radiation does not cause precipitation of additional molybdates or cationic substitution, but amorphization of some small precipitates is predicted to occur following the accumulation of defects. This process is minor, with the bulk of crystallites experiencing structural reorganization that causes particles to be more evenly distributed, and powellite CS to decrease in parallel to a unit cell expansion. Despite a non-linear trend with respect to fluence, Ca and Mo migration, changes to the connectivity of network formers, along with powellite CS and cell parameter changes reach a saturation in modification around 8×10^{13} ions/cm², at which point it can be assumed that every part of the system has been damaged despite ongoing localized changes. The formation of this saturation zone implies competing processes induced by irradiation between accumulated defects, and annealing of said defects by overlapping ion tracks that replicated thermal-like processes. This conclusion indicates that while the mechanism of alteration may involve various structural changes, an average damage structure can be predicted for these compositions during long-term storage of nuclear waste. Furthermore, the results support the durability of a powellite phase within glassy matrices when subjected to significant external SHI-irradiation damage. This indicates that increased waste loading within

similar frameworks is a possibility for future nuclear waste steams and worthy of further investigation.

Supporting Information. The included file contains raw XRD patterns along with Raman spectra, the trends of which are described in the main text. It also includes the results of TRIM calculations.

Supplementary_Information.pdf (PDF)

Data Availability. The raw/processed data required to reproduce these findings cannot be shared at this time due to technical or time limitations.

Corresponding Author

*kp391@cam.ac.uk

Author Contributions

The manuscript was written through various contributions of all authors and all authors have given approval to the final version of the manuscript. †These authors contributed equally. KP wrote manuscript and performed bulk of synthesis and analysis, of which IF supervised as the group principal investigator. SS and SP aided in discussion of results as part of collaboration between the CEA and the University of Cambridge. CG and IM aided in experiments at the irradiation facility and creation of an appropriate experiment proposal. GL made significant contributions to analysis of XRD data and SF maintained and calibrated Raman equipment.

Funding Sources

University of Cambridge, Department of Earth Sciences and EPSRC (Grant No. EP/K007882/1) for an IDS. Additional financial support provided by FfWG and the Cambridge Philosophical Society.

ACKNOWLEDGMENT

The authors would like to thank the EMIR network for irradiation time. They would also like to acknowledge the assistance of several members in the Department of Earth Sciences (Robin Clarke, Chris Parish, Dr. Iris Buisman) and those from the Department of Material Science and Metallurgy (Lata Sahonta, Rachel Olivier) that aided in access to facilities and sample preparation, as well as training on analytical equipment.

ABBREVIATIONS

GC glass ceramic, CS crystallite size, PS particle size, R7T7 French nuclear waste glass composition, SON68 inactive version of R7T7, T_C crystallization temperature, T_m melting temperature.

REFERENCES

- [1] W.E. Lee, M.I. Ojovan, M.C. Stennett, N.C. Hyatt, Immobilisation of radioactive waste in glasses, glass composite materials and ceramics, *Adv. Appl. Ceram.* 105 (2006) 3–12. doi:10.1179/174367606X81669.
- [2] J. V. Crum, B.J. Riley, L.R. Turo, M. Tang, A. Kossoy, Summary Report: Glass-Ceramic Waste Forms for Combined Fission Products, Richland, 2011.
- [3] A. Horneber, B. Camara, W. Lutze, Investigation on the Oxidation State and The Behaviour of Molybdenum in Silicate Glass, in: *MRS Proc. Sci. Basis Nucl. Waste Manag.* V, Berlin, 1981: p. Vol. 11, 279-288.

- [4] W.J. Weber, R.C. Ewing, C.A. Angell, G.W. Arnold, J.M. Delaye, L.W. Hobbs, D.L. Price, Radiation effects in glasses used for immobilization of high-level waste and plutonium disposition, *J. Mater. Res.* 12 (1997) 1946–1978.
- [5] S. Peugot, J.M. Delaye, C. Jégou, Specific outcomes of the research on the radiation stability of the French nuclear glass towards alpha decay accumulation, *J. Nucl. Mater.* 444 (2014) 76–91. doi:10.1016/j.jnucmat.2013.09.039.
- [6] P. Frugier, C. Martin, I. Ribet, T. Advocat, S. Gin, The effect of composition on the leaching of three nuclear waste glasses: R7T7, AVM and VRZ, *J. Nucl. Mater.* 346 (2005) 194–207. doi:10.1016/j.jnucmat.2005.06.023.
- [7] J.M. Gras, R. Do Quang, H. Masson, T. Lieven, C. Ferry, C. Poinssot, M. Debes, J.M. Delbecq, Perspectives on the closed fuel cycle - Implications for high-level waste matrices, *J. Nucl. Mater.* 362 (2007) 383–394. doi:10.1016/j.jnucmat.2007.01.210.
- [8] G. Calas, M. Le Grand, L. Galois, D. Ghaleb, Structural role of molybdenum in nuclear glasses: an EXAFS study, *J. Nucl. Mater.* 322 (2003) 15–20. doi:10.1016/S0022-3115(03)00277-0.
- [9] M. Magnin, S. Schuller, C. Mercier, J. Trébosc, D. Caurant, O. Majérus, F. Angéli, T. Charpentier, Modification of molybdenum structural environment in borosilicate glasses with increasing content of boron and calcium oxide by ^{95}Mo MAS NMR, *J. Am. Ceram. Soc.* 94 (2011) 4274–4282. doi:10.1111/j.1551-2916.2011.04919.x.
- [10] M.I. Ojovan, W.E. Lee, S.E. Ion, *An Introduction to Nuclear Waste Immobilisation*, Elsevier, 2005. doi:10.1016/B978-008044462-8/50000-4.
- [11] S. Schuller, O. Pinet, A. Grandjean, T. Blisson, Phase separation and crystallization of borosilicate glass enriched in MoO_3 , P_2O_5 , ZrO_2 , CaO , *J. Non. Cryst. Solids.* 354 (2008) 296–300. doi:10.1016/j.jnoncrysol.2007.07.041.

- [12] R. Short, Phase Separation and Crystallisation in UK HLW Vitrified Products, *Procedia Mater. Sci.* 7 (2014) 93–100. doi:10.1016/j.mspro.2014.10.013.
- [13] W.M. Haynes, ed., *CRC Handbook of Chemistry and Physics*, 94th ed., CRC Press, 2013.
- [14] K.B. Patel, B. Boizot, S.P. Facq, G.I. Lampronti, S. Peugeot, S. Schuller, I. Farnan, β -Irradiation Effects on the Formation and Stability of CaMoO_4 in a Soda Lime Borosilicate Glass Ceramic for Nuclear Waste Storage, *Inorg. Chem.* (2017) acs.inorgchem.6b02657. doi:10.1021/acs.inorgchem.6b02657.
- [15] T. Taurines, D. Neff, B. Boizot, Powellite-rich glass-ceramics: A spectroscopic study by EPR and Raman spectroscopy, *J. Am. Ceram. Soc.* 96 (2013) 3001–3007. doi:10.1111/jace.12401.
- [16] D. Caurant, O. Majérus, E. Fadel, M. Lenoir, C. Gervais, O. Pinet, Effect of molybdenum on the structure and on the crystallization of $\text{SiO}_2\text{-Na}_2\text{O-CaO-B}_2\text{O}_3$ glasses, *J. Am. Ceram. Soc.* 90 (2007) 774–783. doi:10.1111/j.1551-2916.2006.01467.x.
- [17] B. Boizot, G. Petite, D. Ghaleb, G. Calas, Radiation induced paramagnetic centres in nuclear glasses by EPR spectroscopy, *Nucl. Instruments Methods Phys. Res. Sect. B Beam Interact. with Mater. Atoms.* 141 (1998) 580–584. doi:10.1016/S0168-583X(98)00102-5.
- [18] Y. Inagaki, H. Furuya, K. Idemitsu, Microstructure of simulated high-level waste glass doped with short-lived actinides, ^{238}Pu and ^{244}Cm , in: *Mat. Res. Soc. Symp. Proc.*, 1992: pp. 199–206.
- [19] J. de Bonfils, S. Peugeot, G. Panczer, D. de Ligny, S. Henry, P.-Y. Noël, A. Chenet, B. Champagnon, Effect of chemical composition on borosilicate glass behavior under irradiation, *J. Non. Cryst. Solids.* 356 (2010) 388–393. doi:10.1016/j.jnoncrysol.2009.11.030.
- [20] W.J. Weber, R.C. Ewing, C.R.A. Catlow, T.D. de la Rubia, L.W. Hobbs, C. Kinoshita, H. Matzke, A.T. Motta, M. Nastasi, E.K.H. Salje, E.R. Vance, S.J. Zinkle, Radiation effects in crystalline

- ceramics for the immobilization of high-level nuclear waste and plutonium, *J. Mater. Res.* 13 (1998) 1434–1484. doi:10.1557/JMR.1998.0205.
- [21] R.C. Ewing, A. Meldrum, L. Wang, S. Wang, Radiation-Induced Amorphization, *Rev. Mineral. Geochemistry.* 39 (2000) 319–361. doi:10.2138/rmg.2000.39.12.
- [22] T. Charpentier, L. Martel, A.H. Mir, J. Somers, C. Jégou, S. Peugot, Self-healing capacity of nuclear glass observed by NMR spectroscopy, *Sci. Rep.* 6 (2016) 25499. doi:10.1038/srep25499.
- [23] M. Toulemonde, E. Paumier, C. Dufour, Thermal spike model in the electronic stopping power regime, *Radiat. Eff. Defects Solids Inc. Plasma Sci. Plasma Technol.* 126 (1993) 201–206. doi:10.1080/10420159308219709.
- [24] S. Gin, P. Jollivet, M. Tribet, S. Peugot, S. Schuller, Radionuclides containment in nuclear glasses: an overview, *Radiochim. Acta.* 0 (2017). doi:10.1515/ract-2016-2658.
- [25] J.-M. Delaye, S. Peugot, G. Bureau, G. Calas, Molecular dynamics simulation of radiation damage in glasses, *J. Non. Cryst. Solids.* 357 (2011) 2763–2768. doi:10.1016/j.jnoncrysol.2011.02.026.
- [26] C. Mendoza, S. Peugot, T. Charpentier, M. Moskura, R. Caraballo, O. Bouty, A.H. Mir, I. Monnet, C. Grygiel, C. Jegou, Oxide glass structure evolution under swift heavy ion irradiation, *Nucl. Instruments Methods Phys. Res. Sect. B Beam Interact. with Mater. Atoms.* 325 (2014) 54–65. doi:10.1016/j.nimb.2014.02.002.
- [27] S. Peugot, T. Fares, E. a. Maugeri, R. Caraballo, T. Charpentier, L. Martel, J. Somers, A. Janssen, T. Wiss, F. Rozenblum, M. Magnin, X. Deschanel, C. Jégou, Effect of $^{10}\text{B}(n, \alpha)^7\text{Li}$ irradiation on the structure of a sodium borosilicate glass, *Nucl. Instruments Methods Phys. Res. Sect. B Beam Interact. with Mater. Atoms.* 327 (2014) 22–28. doi:10.1016/j.nimb.2013.09.042.
- [28] A.H. Mir, I. Monnet, B. Boizot, C. Jegou, S. Peugot, Electron and electron-ion sequential

- irradiation of borosilicate glasses: Impact of the pre-existing defects, *J. Nucl. Mater.* 489 (2017) 91–98. doi:10.1016/j.jnucmat.2017.03.047.
- [29] J.F. Ziegler, M.D. Ziegler, J.P. Biersack, SRIM - The stopping and range of ions in matter (2010), *Nucl. Instruments Methods Phys. Res. Sect. B Beam Interact. with Mater. Atoms.* 268 (2010) 1818–1823. doi:10.1016/j.nimb.2010.02.091.
- [30] R.W. Cheary, A. a. Coelho, J.P. Cline, Fundamental parameters line profile fitting in laboratory diffractometers, *J. Res. Natl. Inst. Stand. Technol.* 109 (2004) 1–25. doi:10.6028/jres.109.002.
- [31] K.B. Patel, B. Boizot, S.P. Facq, S. Peugot, S. Schuller, I. Farnan, Impacts of composition and beta irradiation on phase separation in multiphase amorphous calcium borosilicates, *J. Non. Cryst. Solids.* 473 (2017) 1–16. doi:10.1016/j.jnoncrysol.2017.06.018.
- [32] L. Chen, W. Yuan, S. Nan, X. Du, D.F. Zhang, P. Lv, H.B. Peng, T.S. Wang, Study of modifications in the mechanical properties of sodium aluminoborosilicate glass induced by heavy ions and electrons, *Nucl. Instruments Methods Phys. Res. Sect. B Beam Interact. with Mater. Atoms.* 370 (2016) 42–48. doi:10.1016/j.nimb.2016.01.007.
- [33] M. Crane, R.L. Frost, P.A. Williams, J.T. Klopogge, Raman spectroscopy of the molybdate minerals chillagite (tungsteinian wulfenite-I4), stolzite, scheelite, wolframite and wulfenite, *J. Raman Spectrosc.* 33 (2002) 62–66. doi:10.1002/jrs.820.
- [34] S.P.S. Porto, J.F. Scott, Raman spectra of CaWO_4 , SrWO_4 , CaMoO_4 , and SrMoO_4 , *Phys. Rev.* 157 (1967) 716–719. doi:10.1103/PhysRev.157.716.
- [35] E. Sarantopoulou, C. Raptis, S. Ves, D. Christofilos, G.A. Kourouklis, Temperature and pressure dependence of Raman-active phonons of CaMoO_4 : an anharmonicity study, *J. Physics-Condensed Matter.* 14 (2002) 8925–8938. doi:10.1088/0953-8984/14/39/302.

- [36] Z. Zhao, Z. Sui, X. Wei, J. Zuo, X. Zhang, R. Dai, Z. Zhang, Z. Ding, Structure transformation and remarkable site-distribution modulation of Eu^{3+} ions in $\text{CaMoO}_4 : \text{Eu}^{3+}$ nanocrystals under high pressure, *CrystEngComm*. 17 (2015) 7905–7914. doi:10.1039/C5CE01580D.
- [37] T. Taurines, B. Boizot, Microstructure of powellite-rich glass-ceramics: A model system for high level waste immobilization, *J. Am. Ceram. Soc.* 95 (2012) 1105–1111. doi:10.1111/j.1551-2916.2011.05015.x.
- [38] N. Chouard, D. Caurant, O. Majérus, J.L. Dussossoy, S. Klimin, D. Pytalev, R. Baddour-Hadjean, J.P. Pereira-Ramos, Effect of MoO_3 , Nd_2O_3 , and RuO_2 on the crystallization of soda–lime aluminoborosilicate glasses, *J. Mater. Sci.* 50 (2015) 219–241. doi:10.1007/s10853-014-8581-9.
- [39] D. Caurant, O. Majérus, E. Fadel, A. Quintas, C. Gervais, T. Charpentier, D. Neuville, Structural investigations of borosilicate glasses containing MoO_3 by MAS NMR and Raman spectroscopies, *J. Nucl. Mater.* 396 (2010) 94–101. doi:10.1016/j.jnucmat.2009.10.059.
- [40] N. Henry, P. Deniard, S. Jobic, R. Brec, C. Fillet, F. Bart, A. Grandjean, O. Pinet, Heat treatments versus microstructure in a molybdenum-rich borosilicate, *J. Non. Cryst. Solids*. 333 (2004) 199–205. doi:10.1016/j.jnoncrysol.2003.09.055.
- [41] D.R. Neuville, L. Cormier, B. Boizot, A.M. Flank, Structure of β -irradiated glasses studied by X-ray absorption and Raman spectroscopies, *J. Non. Cryst. Solids*. 323 (2003) 207–213. doi:10.1016/S0022-3093(03)00308-9.
- [42] R.L. Frost, J. Bouzaid, I.S. Butler, Raman spectroscopic study of the molybdate mineral szenicsite and compared with other paragenetically related molybdate minerals, *Spectrosc. Lett.* 40 (2007) 603–614.
- [43] J. Goubeau, H. Kellaer, RAMAN-Spektren und Struktur von Boroxol-Verbindungen (German), *ZAAC (Journal Inorg. Gen. Chem.* 272 (1953) 303–312. doi:10.1002/zaac.19532720510.

- [44] J. Krogh-Moe, The structure of vitreous and liquid boron oxide, *J. Non. Cryst. Solids*. 1 (1969) 269–284. doi:10.1016/0022-3093(69)90025-8.
- [45] W.L. Konijnendijk, J.M. Stevels, The structure of borate glasses studied by Raman scattering, *J. Non. Cryst. Solids*. 18 (1975) 307–331. doi:10.1016/0022-3093(75)90137-4.
- [46] W.L. Konijnendijk, *The Structure of Borosilicate Glasses*, Technische Hogeschool Eindhoven, 1975. doi:10.6100/IR146141.
- [47] T. Furukawa, W.B. White, Raman spectroscopic investigation of sodium borosilicate glass structure, *J. Mater. Sci.* 16 (1981) 2689–2700. doi:10.1007/BF00552951.
- [48] B. Hehlen, D.R. Neuville, Raman response of network modifier cations in alumino-silicate glasses, *J. Phys. Chem. B*. 119 (2015) 4093–4098. doi:10.1021/jp5116299.
- [49] G. Battaglin, G.W. Arnold, G. Mattei, P. Mazzoldi, J.-C. Dran, Structural modifications in ion-implanted silicate glasses, *J. Appl. Phys.* 85 (1999) 8040–8049. doi:10.1063/1.370640.
- [50] K. Jurek, O. Gedeon, Volume and composition surface changes in alkali silicate glass irradiated with electrons, *Microchim. Acta*. 161 (2008) 377–380. doi:10.1007/s00604-008-0941-1.
- [51] X. Wang, G. Panczer, D. de Ligny, V. Motto-Ros, J. Yu, J.L. Dussossoy, S. Peugot, I. Jóźwik-Biala, N. Béreud, J. Jagielski, Irradiated rare-earth-doped powellite single crystal probed by confocal Raman mapping and transmission electron microscopy, *J. Raman Spectrosc.* 45 (2014) 383–391. doi:10.1002/jrs.4472.
- [52] W.J. Weber, R.C. Ewing, L.M. Wang, The radiation-induced crystalline-to-amorphous transition in zircon, *J. Mater. Res.* 9 (1994) 688–698. doi:10.1557/JMR.1994.0688.
- [53] H.M. Naguib, R. Kelly, Criteria for bombardment-induced structural changes in non-metallic solids, *Radiat. Eff.* 25 (1975) 1–12. doi:10.1080/00337577508242047.

- [54] K. Trachenko, Understanding resistance to amorphization by radiation damage, *J. Phys. Condens. Matter.* 16 (2004) R1491–R1515. doi:10.1088/0953-8984/16/49/R03.
- [55] R.C. Ewing, W.J. Weber, F.W. Clinard, Radiation effects in nuclear waste forms for high-level radioactive waste, *Prog. Nucl. Energy.* 29 (1995) 63–127. doi:10.1016/0149-1970(94)00016-Y.
- [56] X. Orlhac, C. Fillet, P. Deniard, A.M. Dulac, R. Brec, Determination of the crystallized fractions of a largely amorphous multiphase material by the Rietveld method, *J. Appl. Crystallogr.* 34 (2001) 114–118. doi:10.1107/S0021889800017908.
- [57] S.N. Achary, S.J. Patwe, M.D. Mathews, A.K. Tyagi, High temperature crystal chemistry and thermal expansion of synthetic powellite (CaMoO_4): A high temperature X-ray diffraction (HT-XRD) study, *J. Phys. Chem. Solids.* 67 (2006) 774–781. doi:10.1016/j.jpcs.2005.11.009.
- [58] A. Abdel-Rehim, Thermal Analysis and X-ray Diffraction of Synthesis of Scheelite, *J. Therm. Anal. Calorim.* 64 (2004) 557–569. <http://dx.doi.org/10.1023/A:1011577903726>.
- [59] J. Jagielski, L. Thomé, Multi-step mechanism of damage accumulation in irradiated crystals, *Nucl. Instruments Methods Phys. Res. Sect. B Beam Interact. with Mater. Atoms.* 266 (2008) 1212–1215. doi:10.1016/j.nimb.2007.12.097.
- [60] R.M. Hazen, L.W. Finger, J.W.E. Mariathasan, High-pressure crystal chemistry of scheelite-type tungstates and molybdates, *J. Phys. Chem. Solids.* 46 (1985) 253–263. doi:10.1016/0022-3697(85)90039-3.